# Sub-mm observations and modelling of Vega type stars

I. Sheret[1]⋆, W. R. F. Dent[2] and M. C. Wyatt[2]

[1] *Institute for Astronomy, University of Edinburgh, Royal Observatory, Blackford Hill, Edinburgh, EH9 3HJ*

[2] *UK Astronomy Technology Centre, Royal Observatory, Blackford Hill, Edinburgh, EH9 3HJ*

**ABSTRACT**

We present new sub-mm observations of Vega excess stars, and consistent modelling for all known Vega excess stars with sub-mm data. Our analysis uses dust grain models with realistic optical properties, with the aim of determining physical parameters of the unresolved disks from just their SEDs. For the resolved targets, we find that different objects require very different dust grain properties in order to simultaneously fit the image data and SED. Fomalhaut and Vega require solid dust grains, whilst HR4796 and HD141569 can only be fitted using porous grains. The older stars tend to have less porous grains than younger stars, which may indicate that collisions in the disks have reprocessed the initially fluffy grains into a more solid form. $\epsilon$ Eri appears to be deficient in small dust grains compared to our best fitting model. This may show that it is important to include all the factors which cause the size distribution to depart from a simple power law for grains close to the radiation pressure blowout limit. Alternatively, this discrepancy may be due to some external influence on the disk (e.g. a planet).

When the model is applied to the unresolved targets, an estimate of the disk size can be made. However, the large diversity in dust composition for the resolved disks means that we cannot make a reliable assumption as to the composition of the grains in an unresolved disk, and there is corresponding uncertainty in the disk size. In addition, the poor fit for $\epsilon$ Eri shows that the model cannot always account for the SED even if the disk size is known. These two factors mean that it may not be possible to determine a disk's size without actually resolving it.

**Key words:** circumstellar matter – dust.

## 1 INTRODUCTION

In 1983, the *IRAS* satellite detected a large infrared excess from Vega ($\alpha$ Lyr) during a routine calibration observation (Aumann et al. 1984). Soon, a similar excess was detected from three more stars ($\beta$ Pic, Fomalhaut and $\epsilon$ Eri). The excess could only be explained by a shell or ring of dust, heated to between 50 and 125 K by the central star. Quite by accident, *IRAS* had uncovered the first examples of solid material orbiting a normal main sequence star other that our own Sun.

The four stars mentioned above have become the prototypes for the 'Vega excess' phenomenon (Backman & Paresce 1993; Lagrange, Backman & Artymowicz 2000). A systematic study of the *IRAS* all-sky survey shows that around 15 per cent of all main-sequence stars have an IR excess due to circumstellar dust (Dominik & The Hjhvega Consortium 1997; Fajardo-Acosta et al. 1999). Coronographic and sub-mm imaging has shown the dust is typically in a

ring or disk geometry (Smith & Terrile 1984; Holland et al. 1998) and that these systems have much in common with our own solar system, i.e. solid material in stable coplanar orbits distributed within a region roughly the size of the Kuiper belt.

Though the Vega phenomenon is common, the poor resolution of current far-IR and sub-mm instruments means that few Vega excess stars are close enough to be resolved. For the cases where the disks are resolved, detailed analysis using realistic models for the optical properties and size distribution of the dust can be performed. This type of work has been attempted for $\beta$ Pic (Li & Greenberg 1998a), HR4796 (Augereau et al. 1999b; Li & Lunine 2003a) and Fomalhaut (Wyatt & Dent 2002). These models use the observed spatial distribution of dust, and fit the SED by varying the dust composition and size distribution. However, as these objects have been analysed on a case-by-case basis, different models and assumptions are used, which makes it somewhat difficult to make direct comparisons. In addition, there are so few resolved targets that it is impossible to look for statistical trends between disk size, age, stellar mass, etc. However,

⋆ E-mail: is@roe.ac.uk

there are many unresolved targets with good SED information, and new instruments such as SIRTF and SOFIA will produce many more such objects. A method which could retrieve the physical parameters of a disk from just its SED would be invaluable. To accomplish this, the detailed properties of the dust grains in Vega excess disks must be fully understood.

We have tried to tackle these problems in two ways. Firstly, we have made sub-mm photometric observations of Vega excess stars, to help constrain their SEDs. Secondly, we have attempted to model all known Vega excess stars with sub-mm data, using a consistent model with realistic dust grains. This allows us to directly compare the results of modelling for resolved targets, and use the knowledge of dust grain size and composition gained to estimate the disk size for the unresolved targets.

## 2 OBSERVATIONS

Sub-mm observations were made using the SCUBA bolometer array on the James Clerk Maxwell Telescope. The observations were made as part of several different observing programmes, and hence data was obtained in different observing modes. In addition, we have reduced unpublished archive observations of suspected Vega-excess stars to enlarge our sample. The observations are summarised in Table 1.

SCUBA can be used in two ways, either for photometry or for mapping. The distinction arises because the bolometers are spaced too widely to fully sample the image at the focal plane. Therefore in mapping mode, the moving secondary mirror is used to add slight offsets to the telescope pointing, and hence fill in the gaps in the map. Whilst this is ideal for extended sources, for an observation of an unresolved object a lot of time is spent where no bolometer can see the source. To prevent wasting observation time in this way photometry mode can be used, which does not attempt to make a fully sampled map. In this mode, the central bolometer is always on source, and hence the observation will be more sensitive. The disadvantage is that a fully sampled map is not produced, so if the object is resolved the measured flux will underestimate the true flux. This mode should therefore only be used if the target is known to be point-like. Although a full jiggle map is not used in this mode, a small 9-point map is used to prevent small pointing errors from affecting the measurement.

For some of the observations an extended photometry mode was used, which used a 9-point map with a spacing of 5 arcsec between each point, instead of the normal 2 arcsec spacing. The aim of this was to ensure that the true flux was measured even if the source was marginally resolved, whilst retaining most of the sensitivity advantage of photometry mode. Also, some data was taken using a 12-point pattern, with four points at the centre and eight points arranged around the central position, at a distance of 7 arcsec. Data from these extended photometry modes were reduced in exactly the same way as the conventional photometry.

| Object | Date | Wavelength ($\mu$m) | Mode |
|---|---|---|---|
| HD17206 | 23 Aug 1997 | 450/850 | Map |
| | 27 Aug 1997 | 450/850 | Map |
| | 10 Mar 2001 | 450/850 | Ext. Phot. |
| HD23362 | 7 Jun 2000 | 450/850 | Map |
| HD34282 | 25 Sep 1997 | 450/850 | Map |
| | 29 Jan 2000 | 450/850 | Map |
| | 21 Mar 2000 | 450/850 | Map |
| HD34700 | 14 Aug 1997 | 1350 | Phot |
| | 13 Dec 1997 | 450/850 | Map |
| | 14 Dec 1997 | 450/850 | Map |
| | 11 Feb 1998 | 1350 | Phot |
| | 29 Jan 2000 | 450/850 | Phot |
| HD35187 | 13 Dec 1997 | 450/850 | Map |
| | 14 Jan 1998 | 450/850 | Map |
| HD38393 | 11 Mar 2001 | 450/850 | Ext. Phot. |
| | 12 Mar 2001 | 450/850 | Ext. Phot. |
| HD48682 | 9 Mar 2001 | 450/850 | Ext. Phot. |
| | 10 Mar 2001 | 450/850 | Ext. Phot. |
| | 11 Mar 2001 | 450/850 | Ext. Phot. |
| | 12 Mar 2001 | 450/850 | Ext. Phot. |
| HD69830 | 9 Mar 2001 | 450/850 | Ext. Phot. |
| HD81515 | 21 Mar 2000 | 450/850 | Map |
| HD109085 | 21 Mar 2000 | 450/850 | Map |
| | 10 Mar 2001 | 450/850 | Ext. Phot. |
| | 11 Mar 2001 | 450/850 | Ext. Phot. |
| | 12 Mar 2001 | 450/850 | Ext. Phot. |
| HD121617 | 19 Feb 1998 | 1350 | Photometry |
| | 11 Jun 2000 | 450/850 | Photometry |
| HD123160 | 9 Dec 1997 | 450/850 | Photometry |
| | 19 Feb 1998 | 450/850 | Photometry |
| | 10 Jun 2000 | 450/850 | Map |
| HD128167 | 21 Jan 2002 | 450/850 | Ext. Phot. |
| HD139664 | 30 Nov 1997 | 450/850 | Map |
| | 13 May 1998 | 450/850 | Map |
| | 25 Jun 1998 | 450/850 | Map |
| | 11 Jun 2000 | 450/850 | Photometry |
| HD141569 | 18 Feb 1998 | 1350 | Photometry |
| | 19 Feb 1998 | 1350 | Photometry |
| | 4 May 1998 | 1350 | Photometry |
| | 13 Jan 1999 | 1350 | Photometry |
| | 10 Jun 2000 | 450/850 | Photometry |
| | 11 Jun 2000 | 450/850 | Phot |
| HD207129 | 17 May 1998 | 450/850 | Map & Phot |
| | 28 May 1998 | 450/850 | Map |

**Table 1.** New observations used in our analysis. Observations before 2000 were extracted from the JCMT archive. The extended photometry of HD128167 was observed with a 12 point pattern, all other extended photometry is 9 point.

## 3 DATA REDUCTION

### 3.1 Photometry data

Photometry data were reduced using the SURF package. After combining the positive and negative beams, the data were flat-fielded and corrected for atmospheric extinction, estimated using a polynomial fit to the CSO 225 GHz opacity monitor and the relations in Archibald, Wagg & Jenness (2000). Residual sky emission was estimated using bolometers well separated from the source, and this signal was subtracted from the data. The sky bolometers were those in rings 2 and 3 (30 bolometers in total), and their median was

| Object | Other name | Spectral type | Distance pc | $L_{\mathrm{dust}}/L_{\mathrm{star}}$ | Reference | Estimated age Myr | Reference |
|---|---|---|---|---|---|---|---|
| HD17206 | | F5/F6V | 13.97 | | | | |
| HD23362 | | K2 | 308.6 | $7.9 \times 10^{-4}$ | 1 | | |
| HD34282 | | A0 | 163.9 | 0.39 | 1 | | |
| HD34700 | | G0 | $>180$ | 0.14 | 2 | | |
| HD35187 | | A2 | 150 | 0.14 | 1 | | |
| HD38393 | | F7V | 8.97 | $5.3 \times 10^{-6}$ | Best fit model | $1660^{+1580}_{-1391}$ | 8 |
| HD48682 | | G0V | 16.4 | $1.2 \times 10^{-4}$ | Best fit model | | |
| HD69830 | | K0V | 12.58 | $2.3 \times 10^{-4}$ | Spline | 600-2000 | 10 |
| HD81515 | | A5Vm... | 107.0 | | | | |
| HD109085 | | F2V | 18.2 | $4 \times 10^{-4}$ | Spline | | |
| HD121617 | | A1V | $180^a$ | $4.5 \times 10^{-3}$ | 2 | | |
| HD123160 | | K5 | $>250$ | | | | |
| HD128167 | $\sigma$ Boo | F2V | 15.5 | $1.8 \times 10^{-5}$ | Best fit model | $1700^{+1320}_{-720}$ | 8 |
| HD139664 | | F5IV-V | 17.5 | $1.9 \times 10^{-4}$ | Spline | $1120^{+880}_{-875}$ | 8 |
| HD141569 | | B9 | 99.0 | $8.3 \times 10^{-3}$ | 2 | $5 \pm 3$ | 7 |
| HD207129 | | G0V | 15.6 | $1.0 \times 10^{-4}$ | Spline | $6030^{+2290}_{-1660}$ | 8 |
| HD22049 | $\epsilon$ Eri | K2V | 3.22 | $1.1 \times 10^{-4}$ | Best fit model | $730 \pm 200$ | 10 |
| HD39060 | $\beta$ Pic | A5V | 19.3 | $3 \times 10^{-3}$ | 3 | $20 \pm 10$ | 6 |
| HD109573 | HR4796 | A0V | 67 | 0.005 | 4 | $8 \pm 2$ | 9 |
| HD172167 | Vega | A0V | 7.76 | $2 \times 10^{-5}$ | 3 | $354^{+29}_{-87}$ | 5 |
| HD216956 | Fomalhaut | A3V | 7.69 | $8 \times 10^{-5}$ | 3 | $156^{+188}_{-106}$ | 5 |

Reference list: 1 Sylvester et al. (1996); 2 Sylvester, Dunkin & Barlow (2001); 3 Backman & Paresce (1993); 4 Jura (1991); 5 Song et al. (2001); 6 Barrado y Navascués et al. (1999); 7 Weinberger et al. (2000); 8 Lachaume et al. (1999); 9 Stauffer, Hartmann & Barrado y Navascues (1995); 10 Song et al. (2000).

$^a$No parallax was available, so the distance was estimated by assuming the absolute visual magnitude for a A1V star is +1.0 (Lang 1992, page 144), and using the measured visual magnitude of 7.298 from SIMBAD.

**Table 2.** Parameters of stars used in our analysis. The top part of the table shows objects with new sub-mm data, the bottom part shows objects where we have analysed published data. Spectral type and distance are from SIMBAD.

taken as the average sky signal. The signal from the central bolometer was then despiked using a 4 sigma cut.

Calibration sources were observed and reduced in exactly the same way as the targets. If a planet was used as a calibrator, the FLUXES package was used to estimate the flux and a correction was made for the loss of flux because the object was resolved. For the observations taken with the extended photometry mode, all of the calibration sources were point-like (i.e. secondary calibrators, not planets). Thus the final photometry is derived under the assumption that the emission is point-like and centred on the star. If a target is extended (i.e. marginally resolved) or is offset from the position of the star, then observations in photometry mode will underestimate the true flux, by an amount shown in Table 3. As expected, the extended photometry modes are less affected than the conventional photometry mode.

| Offset arcsec | FWHM arcsec | Relative response | | |
|---|---|---|---|---|
| | | Normal | Ext. 9 pt. | Ext. 12 pt. |
| 0 | 0 | 1.00 | 1.00 | 1.00 |
| 0 | 5 | 0.89 | 0.93 | 0.92 |
| 0 | 10 | 0.68 | 0.76 | 0.75 |
| 5 | 0 | 0.72 | 0.81 | 0.79 |
| 5 | 5 | 0.67 | 0.76 | 0.75 |
| 5 | 10 | 0.54 | 0.65 | 0.63 |
| 10 | 0 | 0.27 | 0.41 | 0.40 |
| 10 | 5 | 0.28 | 0.41 | 0.39 |
| 10 | 10 | 0.28 | 0.39 | 0.37 |

**Table 3.** Comparison of the three photometry modes, showing effect of an extended or offset Gaussian source. The table shows the ratio of the quoted flux density to the true flux density. The PSF FWHM is assumed to be 14 arcsec.

### 3.2 Maps

Map data was reduced using custom data reduction software written in IDL. This system is similar to that developed to reduce data for the 8-mJy extragalactic survey (Scott et al. 2002). This method is preferred over the SURF software because the residual sky emission is removed more effectively (a plane is fitted to the residual emission, rather than a constant), and the 'zero footprint' rebinning method produces a map where each pixel is an independent measurement, which makes subsequent analysis much simpler. Source flux was measured by fitting an elliptical Gaussian to the source.

To ensure that the software was reliable, SURF was used to reduce several sources, and the results from the two reduction systems were compared to ensure that any differences were well within the errors.

Calibration was done by calculating the flux conversion factor from the peak flux of a Gaussian fit to calibration sources. Using the peak signal rather than the integrated signal means that the measurement is sensitive to changes in the beam shape (Dunne & Eales 2001), but this approach was necessary as most of the calibration sources were sec-

ondary calibrators, and only the peak signal is well determined for these sources.

## 4   RESULTS

The results of the sub-mm observations are shown in Table 4. For objects with multiple observations, the flux given is the weighted mean of all the data. Of the 15 objects observed, 7 were not detected, 4 were detected at 850 $\mu$m and 450 $\mu$m, and 4 were detected at 850 $\mu$m only.

Most of the objects have not been observed in the sub-mm before, but for objects with existing observations, the new data were checked for consistency with the old results. HD34282 and HD35187 have both been observed with UKT14 (Sylvester et al. 1996): HD34282 had a flux of $1.3 \pm 0.3$ Jy at 400 $\mu$m and $0.409 \pm 0.027$ Jy at 800 $\mu$m, HD35187 had a flux of $0.115 \pm 0.022$ Jy at 800 $\mu$m. The discrepancy between these fluxes and the new data is small (2 sigma), however similar discrepancies have been found in other comparisons of UKT14 and SCUBA data (e.g. Sylvester et al. 2001). This may be due to calibration errors in the original data.

For the purposes of this paper, the extended photometry observations have been reduced in exactly the same way as conventional photometry, so the result of the data reduction is just the total flux. However, the data also contains some spatial information, and more complicated reduction will give some indication of the size of the disk as well as its flux. This will be tackled in subsequent paper (Wyatt et al., in preparation).

One of the advantages of SCUBA observations is that they can confirm the *IRAS* excess is associated with the star, and not simply a background source (i.e. a galaxy or galactic cirrus). Contamination by background sources is a significant problem, and follow up observations are important to confirm that the *IRAS* associations are real. Certainly, not all *IRAS* associations are real, as demonstrated by observations of 55 Cnc (Jayawardhana et al. 2002) and HD155826 (Lisse et al. 2002). SCUBA is a useful tool for confirming associations because it gives source positions which are significantly more accurate than those from *IRAS*. *IRAS* detections have a typical positional uncertainty of about 16 arcsec in the cross-scan direction and 3 arcsec in the in-scan direction (Beichman et al. 1988). In map mode, SCUBA positional uncertainties are about 2 arcsec for bright sources, limited only by the pointing accuracy of the dish. In photometry mode, the positional accuracy is determined by the size of the beam (FWHM of 14 arcsec) so these observations are less useful for this purpose. From our sample, one object was rejected on the basis of it's sub-mm position: HD123160 was a strong SCUBA detection, but the source seemed to be offset from the stellar position by about 10 arcsec. In addition, this star is now thought to be a distant class III giant (Kalas et al. 2002), and there is evidence of several galaxies in the optical DSS survey image. This indicates that the *IRAS* source is probably a background galaxy.

SCUBA is also sensitive to background galaxies, and so there is a possibility that a background galaxy could fall into the beam of the observations and cause a spurious detection. The chances of this happening depend on the limiting flux of the observations (as there are many more faint galaxies than

bright ones) and the size of the beam. The extended photometry mode is therefore more susceptible to this problem, as it is sensitive to sources over $\sim 2$ times more area than conventional photometry. The tentative detection of HD38393 has the highest probability of being due to a background galaxy, as the source is extremely faint and the observations were taken in extended photometry mode. This possibility is discussed further in Section 6.8.

The mass of the disks was estimated from the 850 $\mu$m flux, using a dust temperature determined from the peak of the dust emission SED, and this is shown in Table 4. We set the mass absorption coefficient $\kappa = 1.7$ cm$^2$ g$^{-1}$ at 850 $\mu$m for consistency with previous work (e.g. Zuckerman & Becklin 1993; Holland et al. 1998; Sylvester et al. 2001). Detailed discussion of the value of $\kappa$ can be found in Pollack et al. (1994). It is important to note that this mass estimate cannot measure the mass held in grains larger than about 1 mm. This is a key point, as in a collisional cascade (see Section 5.3), the total mass of the disk is dominated by the contribution from large bodies, which contribute little to the 850 $\mu$m emission. Our mass estimate only reflects the amount of mass held in small dust grains, and even then is model dependent. The dust masses of the new targets are comparable with those measured in previous studies, ranging from 0.04 lunar masses (HD38393) to 33 lunar masses (HD141569) for the Vega excess stars, and hundreds of lunar masses or more for the pre-main-sequence stars (HD34700, HD35187 and HD34282).

## 5   SED MODELLING

Our key objective is to determine the size of a Vega excess disk from just its SED. Because models have many free parameters, we have tried to constrain as much as possible using our understanding of the physical processes taking place in the disks, in particular by setting the size distribution from theoretical arguments.

The model used here is a modified version of the model developed to fit the SED and sub-mm image of Fomalhaut (Wyatt & Dent 2002), and a more detailed description can be found there. The model is based on a collisional cascade, where small dust grains are continuously created by collisions between larger bodies. The only significant difference between the model used here and that used in Wyatt & Dent (2002) is that we use a simpler assumption about the spatial distribution of the dust (see Section 5.4 for details).

For this model to be accurate, the disk must be optically thin to radiation from the central star. If this is not the case, then the inner parts of the disk will shadow the outer parts from starlight, and a radiative transfer code would be needed to properly model the system. We have therefore excluded all the objects where $L_{\mathrm{dust}}/L_{\mathrm{star}} > 0.01$. This ensures that disks are optically thin, as long as the opening angle is more than $2°$. Measured opening angles are generally larger than this, e.g. $7°$ for $\beta$ Pic (Heap et al. 2000). HD34282, HD34700, and HD35187 all have $L_{\mathrm{dust}}/L_{\mathrm{star}} > 0.1$, so these objects have not been included in our analysis.

| Object | Flux (Jy) | | $T_{\rm dust}$ | Dust mass |
|--------|-----------|-----------|------|-----------|
| | $450\mu$m | $850\mu$m | K | $M_{\rm moon}$ |
| HD17206 | $< 0.1789$ | $< 0.0078$ | | $< 0.33^a$ |
| HD23362 | $< 0.17$ | $< 0.012$ | | $< 248^a$ |
| HD34282 | $1.925 \pm 0.29$ | $0.384 \pm 0.023$ | | $3 \times 10^{4\ b}$ |
| HD34700 | $0.218 \pm 0.037$ | $0.0407 \pm 0.0024$ | | $> 286^a$ |
| HD35187 | $0.268 \pm 0.047$ | $0.061 \pm 0.005$ | | $298^a$ |
| HD38393 | $< 0.0428$ | $0.0024 \pm 0.001$ | 82 | 0.04 |
| HD48682 | $< 0.0368$ | $0.0055 \pm 0.0011$ | 99 | 0.3 |
| HD69830 | $< 2.0248$ | $< 0.1005$ | | $< 3.5^a$ |
| HD81515 | $< 0.26$ | $< 0.02$ | | $< 49.7^a$ |
| HD109085 | $< 0.0381$ | $0.0075 \pm 0.0012$ | 85 | 0.6 |
| HD121617 | $< 0.36$ | $< 0.012$ | | 85 |
| HD123160$^c$ | $0.152 \pm 0.046$ | $0.021 \pm 0.007$ | | |
| HD139664 | $< 0.39$ | $< 0.015$ | | $< 1.0^a$ |
| HD141569 | $0.066 \pm 0.023$ | $0.014 \pm 0.002$ | 90 | 33 |
| HD207129 | $< 1.7$ | $< 0.018$ | | $< 0.95^a$ |
| $\sigma$ Boo | | $0.0062 \pm 0.0017$ | 62 | 0.5 |
| $\epsilon$ Eri | $0.225 \pm 0.010$ | $0.040 \pm 0.0015$ | 85 | 0.1 |
| $\beta$ Pic | | $0.104 \pm 0.010$ | 103 | 7.8 |
| HR4796 | $0.180 \pm 0.15$ | $0.0191 \pm 0.0034$ | 99 | 19 |
| Vega | | $0.0457 \pm 0.0054$ | 68 | 0.8 |
| Fomalhaut | $0.595 \pm 0.035$ | $0.097 \pm 0.005$ | 75 | 1.7 |

$^a$Calculated assuming a dust temperature of 100 K.
$^b$Taken from Piétu, Dutrey & Kahane (2003).
$^c$Sub-mm emission is offset by 9 arcsec from the star, and is thought
to be due to a galaxy (see Section 4).

**Table 4.** Photometry results and estimated dust masses for our sample. The top part of the table shows new data, the bottom part shows existing data. The dust temperature is estimated from the wavelength of maximum emission for the best fitting SED model. HD34700 only has a lower limit on its distance, and hence we calculate a lower limit on its dust mass. These mass estimates are consistent with existing estimates made for Fomalhaut, Vega, and $\beta$ Pic in Holland et al. (1998) and for $\epsilon$ Eri in Greaves et al. (1998).

| Object | Flux (Jy) | | | |
|--------|-----------|-----------|-----------|-----------|
| | 12 $\mu$m | 25 $\mu$m | 60 $\mu$m | 100 $\mu$m |
| Fomalhaut | $12.1 \pm 1.2$ | $3.9 \pm 0.3$ | $10.0 \pm 0.6$ | $10.7 \pm 0.6$ |
| HR4796 | | $4.2 \pm 0.4$ | $7.1 \pm 0.9$ | $3.6 \pm 0.4$ |
| Vega | $27.8 \pm 1.4$ | $9.3 \pm 0.5$ | $9.8 \pm 0.4$ | $7.6 \pm 0.4$ |
| $\epsilon$ Eri | $6.6 \pm 0.3$ | $2.18 \pm 0.11$ | $1.57 \pm 0.08$ | $1.99 \pm 0.22$ |
| $\beta$ Pic | | $10.6 \pm 0.4$ | $19.1 \pm 0.8$ | $10.4 \pm 0.4$ |
| HD38393 | $3.00 \pm 0.15$ | $0.69 \pm 0.04$ | $0.19 \pm 0.03$ | $< 0.5$ |
| HD48682 | $1.00 \pm 0.06$ | $0.29 \pm 0.03$ | $0.36 \pm 0.05$ | $< 1.0$ |
| HD141569 | | $2.29 \pm 0.05$ | $5.3 \pm 0.8$ | $4.1 \pm 0.5$ |
| $\sigma$ Boo | $1.10 \pm 0.05$ | $0.32 \pm 0.02$ | $0.13 \pm 0.04$ | $< 0.5$ |
| HD207129 | $0.60 \pm 0.03$ | $0.15 \pm 0.02$ | $0.31 \pm 0.04$ | $< 0.24$ |

**Table 6.** Colour corrected *IRAS* fluxes, based on the best fitting model. Upper limits are three sigma, and are taken directly from the *IRAS* faint source catalogue. HD109085 has been excluded because the best fitting model is unlikely to be representative of the true spectral shape at any of the *IRAS* wavelengths.

### 5.1 Photometric data

Mid and far IR photometry data is taken from the *IRAS* faint source catalogue (Moshir et al. 1990). Where available, this is supplemented by ground based mid-IR data from the literature. Also, published *ISO* photometry has been added to help constrain the far-IR part of the SEDs (in particular data from Habing et al. 2001).

### 5.2 Dust grain properties

Our model of the dust grains is based on the assumption that the grains in protoplanetary disks are aggregates of interstellar dust grains, with an additional ice component frozen into them as they grow. This type of model was originally developed to simulate cometary grains (Greenberg 1982, 1998), but it has also been successfully applied to the dust grains in accretion disks (Pollack et al. 1994), and to the debris disks of $\beta$ Pic (Li & Greenberg 1998a), HR4796 (Augereau

| Object | $p$ | $q_{ice}$ | $D_{min}$ $\mu$m | Reduced $\chi^2$ | $R$ AU |
|---|---|---|---|---|---|
| Fomalhaut | 0.0 | | 9.6 | 4.2 | 150 |
| | 0.5 | 0.0 | 18.6 | 14.1 | 150 |
| | 0.9 | 0.0 | 91.0 | 23.2 | 150 |
| | 0.5 | 1.0 | 12.5 | 9.3 | 150 |
| HR4796 | 0.0 | | 10.9 | 16.8 | 70 |
| | 0.5 | 0.0 | 21.3 | 1.8 | 70 |
| | 0.9 | 0.0 | 105.2 | 3.2 | 70 |
| | 0.5 | 1.0 | 14.3 | 25.6 | 70 |
| Vega | 0.0 | | 28.3 | 4.2 | $120 \pm 13$ |
| | 0.5 | 0.0 | 55.9 | 4.9 | $191 \pm 16$ |
| | 0.9 | 0.0 | 281.4 | 4.7 | $237 \pm 21$ |
| | 0.5 | 1.0 | 37.2 | 5.4 | $92 \pm 8$ |
| $\epsilon$ Eri | 0.0 | | 0.74 | 33.6 | 60 |
| | 0.5 | 0.0 | 0.44 | 110.9 | 60 |
| | 0.9 | 0.0 | 0.51 | 139.4 | 60 |
| | 0.5 | 1.0 | 0.67 | 43.7 | 60 |
| | 0.0 | | 3.5 | 2.8 | 60 |
| | 0.0 | | 7.0 | 6.6 | 60 |
| | 0.0 | | 12.0 | 14.0 | 60 |
| $(q = 1.9)$ | 0.0 | 1.0 | 0.74 | 25.6 | 60 |
| $(q = 1.8)$ | 0.0 | 1.0 | 0.74 | 139.4 | 60 |
| $(q = 1.76)$ | 0.0 | 1.0 | 0.74 | 808.9 | 60 |
| $\beta$ Pic | 0.0 | | 5.9 | 12.2 | $43.5 \pm 1.8$ |
| | 0.5 | 0.0 | 11.2 | 13.6 | $62.1 \pm 2.5$ |
| | 0.9 | 0.0 | 53.3 | 11.5 | $82 \pm 3$ |
| | 0.5 | 1.0 | 7.6 | 18.6 | $31.9 \pm 1.1$ |
| HD141569 | 0.0 | | 10.3 | 2.0 | $55.0 \pm 2.3$ |
| | 0.5 | 0.0 | 20.1 | 1.9 | $84 \pm 4$ |
| | 0.9 | 0.0 | 99.5 | 2.4 | $114 \pm 5$ |
| | 0.5 | 1.0 | 13.5 | 3.8 | $43.8 \pm 1.7$ |
| HD109085 | 0.0 | | 4.2 | 4.0 | $180 \pm 40$ |
| HD38393 | 0.0 | | 2.7 | 0.4 | $200 \pm 50$ |
| HD48682 | 0.0 | | 2.3 | 7.0 | $71 \pm 15$[a] |
| | 0.0 | | 2.3 | 3.1 | $110 \pm 21$[b] |
| $\sigma$ Boo | 0.0 | | 3.3 | 2.0 | $320 \pm 90$ |
| HD207129 | 0.0 | | 1.6 | 3.7 | $260 \pm 50$ |

[a] Assuming secondary does not contribute to *IRAS* fluxes
[b] Assuming secondary does contribute to *IRAS* fluxes

**Table 5.** Results of the SED fitting, where $p$ is the porosity of the grains, $q_{ice}$ is the fraction of this porosity filled with ice, and $D_{min}$ is the smallest dust grains in the system. $D_{min}$ was determined by the blowout limit due to radiation pressure, except for $\epsilon$ Eri (see Section 6.3). Where no error is quoted on the disk radius, the size was constrained from existing images and was not a free parameter of the fits.

et al. 1999b; Li & Lunine 2003a), HD141569 (Li & Lunine 2003b) and HD207129 (Jourdain de Muizon et al. 1999).

For the composition of the interstellar grains, we use the core-mantle model developed in Li & Greenberg (1997), which successfully fits the observed interstellar extinction and polarisation. This model has a silicate core surrounded by a UV-processed organic refractory mantle. We force the silicate/organic-refractory volume ratio to be 1:2, as inferred for cometary grains (Greenberg 1998). The grains are assumed to be porous, with the porosity being a free parameter of the model. For dust grains cooler than $\sim 120$ K, the gaps due to porosity may be filled with either vacuum, water ice or a mixture of the two; for dust grains warmer than $\sim 120$ K most ices would sublime, so the gaps must be filled with vacuum. The free parameters in the dust composition model are therefore the porosity $p$ of the grains and the ice fraction $q_{ice}$, with the constraint that for warm grains the ice fraction must be zero.

Optical constants for the materials are taken from Li & Greenberg (1997, 1998a). The optical constants for the composite dust grain material are then calculated using Maxwell-Garnet effective medium theory. Then, the absorption efficiencies for the dust grains are calculated using Mie theory, Rayleigh-Gans theory, or geometric optics, depending on the size of the dust grain. Details of Maxwell-Garnet effective medium theory, and the methods used to calculate absorption efficiencies are discussed in Bohren & Huffman (1983).

### 5.3 Size distribution

The size distribution that results from an infinite collisional cascade is (Dohnanyi 1969):

$$n(D) \propto D^{2-3q} \tag{1}$$

where $n(D)dD$ is the number of planetesimals of size between $D$ and $D + dD$, and $q = 11/6$. However, this distribution will only hold for large dust grains, as radiation pressure will blow out small grains (e.g. $< 1$ $\mu$m) very rapidly, and Poynting-Robertson drag will cause intermediate sized grains (e.g. $< 10$ $\mu$m) to spiral inwards toward the star. Which of these two effects is dominant depends on the optical depth of the dust disk, but for all but the most tenuous disks the collisional timescale is shorter than the PR timescale, so PR drag can be safely ignored (Wyatt et al. 1999). Given this, we assume that the above size distribution holds down to the radiation blowout limit, when $\beta > 0.5$ (where $\beta = F_{rad}/F_{grav}$), at which point there is a sharp cutoff.

### 5.4 Spatial distribution

For the spatial distribution of the dust grains, we assume a infinitely thin, flat ring, with the ring's radius $R$ as a free parameter. This approach is motivated by the sub-mm images of Fomalhaut and $\epsilon$ Eri, which both show a narrow, well defined ring of emitting material. This spatial distribution is different from that used in Wyatt & Dent (2002), as here no attempt is made to account for the eccentricities of the dust grains, which broadens the ring by about 50 AU. The advantage of the simpler model is that it reduces the number of free parameters, but should still give a reasonable estimate of the overall extent of the disk. The Fomalhaut results from the two versions of the model are almost identical (see Section 6.1), which gives us confidence that this simplification will not affect our conclusions.

### 5.5 Stellar parameters

Accurate stellar parameters are needed for several reasons. Firstly, the photospheric flux must be estimated in each band, so that the excess flux due to dust can be determined. This is particularly important in the *IRAS* 12 and 25 $\mu$m bands, where the photosphere can be the dominant source of flux. Secondly, the temperature of the dust depends on the

luminosity of the star, and on the shape of the star's spectrum in the region where most power is emitted (i.e. UV—optical—near-IR). The luminosity and stellar spectrum also determine the magnitude of the radiation forces which act on the dust grains. Finally, an estimate of the mass of the star is needed to calculate the gravitational forces.

To determine the stellar parameters, we first obtained the spectral type of each star from SIMBAD. This was used to estimate the star's effective temperature, using the calibration provided in Gray & Corbally (1994). We then extracted a Kurucz model atmosphere with this effective temperature, assuming solar metallicity and surface gravity $\log(g) = 4.3$ appropriate for dwarf stars. The model atmosphere was then normalised to fit the K band magnitude. K band was preferred over optical photometry because it is less susceptible to the effects of reddening. The luminosity of the star was then calculated by integrating the normalised model atmosphere. Finally, the mass of the star was estimated using the observed spectral type and the table provided by Lang (1992, page 132).

## 5.6 Modelling method

A model SED is specified by the grain composition (porosity $p$, ice fraction $q_{ice}$), radius of the dust ring ($R$), and the total dust luminosity. In the cases where the size of the dust ring is known, the ring radius is fixed to the observed size; for the unresolved objects the ring radius is left as a free parameter. The approach we take is to choose a dust composition, and then find the best fit to the data by varying the remaining free parameters.

The emission spectrum of an individual dust grain depends on its temperature and on the emission efficiency as a function of wavelength. The SED of a disk is simply the combined emission of all the dust grains. For a given dust composition model, the absorption efficiency is calculated as a function of grain size. Given this, the temperature of the dust grains as a function of grain size and distance from the star can be determined. Then, the total flux as a function of wavelength is found by integrating over all grain sizes, weighting with the size distribution given in Equation 1.

The model spectrum is then converted into an SED that can be directly compared to the observed points to obtain a $\chi^2$ value. To do this, the spectral response of each filter-instrument combination is multiplied by the model spectrum, to estimate the broad-band flux that would be recovered from a real observation of the model spectrum. This step is particularly important for the *IRAS* data points, which have a very wide band-pass. By converting the model spectrum into broad-band fluxes, we avoid having to make colour-correction to the original data, which would otherwise require detailed knowledge of the true spectrum of the source. However, when showing the result of the fit, a colour-correction must be applied so that the data points can be plotted in real units. For this purpose, the best fitting model is used to estimate the colour correction for each point. If the best model is more than 3 sigma away from a data point, then no colour-correction is applied to that point, as the model is not likely to give a good estimate of the true colour-correction.

For some objects it is impossible to fit all the data points simultaneously, because there is dust at a range of distances
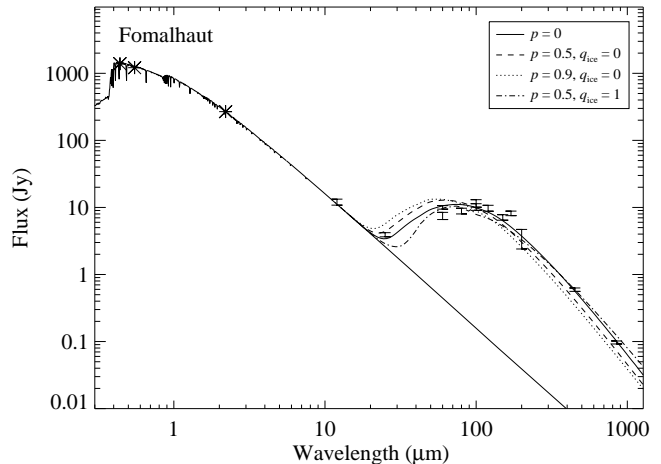


**Figure 1.** SED of Fomalhaut and model fits with the ring radius set at 150 AU. Asterisks show optical and near-IR photometry, *IRAS*, *ISO* and SCUBA data are shown with error bars. Colour corrections for the *IRAS* data were estimated from the $p = 0$ model.

from the star. In these cases, only the long wavelength points are fitted, in order to obtain an estimate of the overall extent of the ring.

## 6 MODELLING RESULTS

### 6.1 Fomalhaut

The size of Fomalhaut's dust disk is known from the sub-mm images made with SCUBA (Holland et al. 2003). Because the ring is inclined and the images have low resolution the size of the ring cannot be measured directly from the images, but the best estimate of the true size is 150 AU (Wyatt & Dent 2002). The SED data for Fomalhaut comes from *IRAS*, SCUBA and also *ISO*. The *ISO* fluxes are from Walker et al. (in preparation), and are listed in Wyatt & Dent (2002).

Our modelling (Figure 1) shows a good fit for solid dust grains (i.e. $p = 0.0$), but rules out porous grains as this would make the dust hotter than is observed. The $p = 0.5$, $q_{ice} = 1.0$ model is also ruled out, as it fails to fit the mid-IR part of the SED.

The reduced $\chi^2$ for the best fitting model is 4.2, which indicates that the model is not consistent with the data. However, by far the dominant contribution to $\chi^2$ comes from the *ISO* data, which show considerable scatter from any smooth model. The *ISO* filters all have broad band passes ($\Delta\lambda/\lambda \sim 0.5$), so the apparent scatter in the *ISO* points is unlikely to be due to structure in the spectrum. A more likely explanation is that uncertainties on the *ISO* points have been underestimated, and this would explain the high reduced $\chi^2$.

Fomalhaut has already been modelled in detail by Wyatt & Dent (2002), and the results here are almost identical to those results. As the modelling here uses the same data and dust grain model, it is hardly surprising that we recover the same results. However, this does confirm that the simpler spatial distribution used here does not significantly affect the results of the modelling.
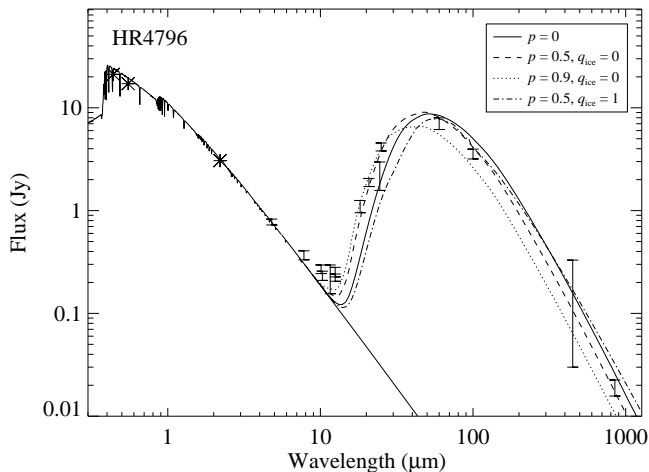
**Figure 2.** SED of HR4796 and model fits with the ring radius set at 70 AU. Data where the wavelength is shorter than 18 $\mu$m has been excluded from the fit, as the excess here is probably due to a hot dust component close to the star (see Section 6.2). Upper limits are 3 sigma. Colour corrections for the *IRAS* data were estimated from the $p = 0.5$, $q_{ice} = 0$ model.

## 6.2  HR4796

HR4796 is resolved in both mid-IR images of dust emission (Jayawardhana et al. 1998; Koerner et al. 1998) and scattered light images in the near-IR (Schneider et al. 1999). The best estimate of the size of the ring comes from mid-IR images, which suggest that the radius is 70 AU. The star is younger than most of the other stars in the sample, with an age of $8 \pm 2$ Myr (Stauffer et al. 1995).

The modelling results show that solid dust grains are unable to fit the observed SED and disk size (Figure 2). However, using a porosity of $p = 0.5$ provides a good fit to the SED. The icy model ($p = 0.5$, $q_{ice} = 1.0$) is a worse fit than the solid grain model, so can be rejected. Around 10 $\mu$m, there is an additional excess which cannot be accounted for by any model. This is likely to be produced by a hot dust component close to the star. Data in this part of the spectrum have therefore been excluded from the fit, and do not contribute to the total $\chi^2$ quoted in Table 5.

Detailed modelling of this object has been done previously by Augereau et al. (1999b), and our results here are in good agreement with this work. Augereau et al. made a much more thorough exploration of parameter space, but their overall conclusion was that two dust populations are required: a cool component at 70 AU, and a hotter component at about 10 AU. Their best fitting model for the cool dust has amorphous grains with a porosity of $p = 0.6$ and an ice fraction ice $q_{ice} = 0.03$. In their analysis, the ring's diameter was constrained to be 70 AU, but the grain porosity, ice fraction and the width of the dust ring were all left as free parameters. As for Fomalhaut, our results confirm that the simpler model used here is able to produce similar results to a more detailed model.

Modelling of HR4796 has also been done by Li & Lunine (2003a), and they were able to fit the entire SED without having a hot dust component, in contrast to the results of Augereau et al. (1999b) and the results presented here. This
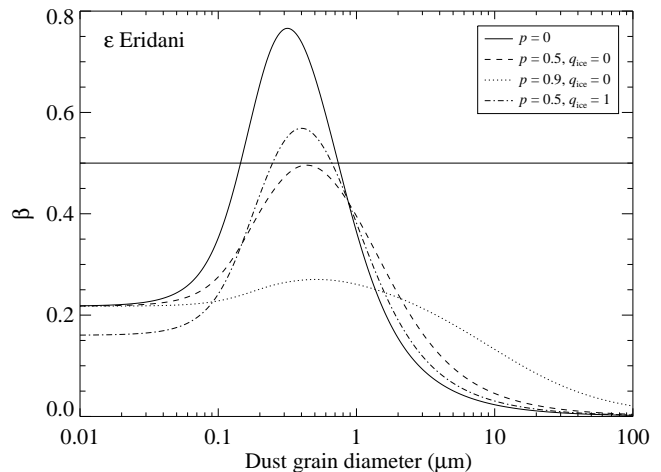


**Figure 3.** Graph showing how $\beta$ ($= F_{rad}/F_{grav}$) depends on dust grain size, for dust orbiting $\epsilon$ Eri. $\beta = 0.5$ is shown by the horizontal line; any dust grain with $\beta > 0.5$ will leave the system on a hyperbolic trajectory.

discrepancy is probably because Li and Lunine's model contains a large number of grains which are much smaller than the blowout diameter, and these small grains produce a hot component in the SED even though they are distant from the central star.

## 6.3  $\epsilon$ Eri

$\epsilon$ Eri is a particularly interesting object, as it is the only cool star (K2V) with a resolved dust disk, all other resolved disks being around A stars. SCUBA images of $\epsilon$ Eri show a distinct ring, which is approximately face on and has a radius of 60 AU (Greaves et al. 1998).

In modelling $\epsilon$ Eri's dust disk, a problem arises due to the low luminosity of the star. Our model for the dust size distribution assumes that radiation pressure will remove the smallest dust grains. However, in the case of $\epsilon$ Eri the radiation pressure is not sufficient to blow dust grains out of the system when porous dust grains are used (Figure 3). In this situation, it is not clear what limits the size of the smallest dust grains. As a first step, we made the ad-hoc assumption that when porous grains were used, the small size cutoff is set at the grain size where $\beta$ is greatest, i.e. where the radiation force is most significant compared to the gravitational force. Modelling using this assumption produced a very interesting result: all of the models predict too much flux in the mid-IR, and too little in the sub-mm (Figure 4). This means that our models have too many small (and therefore hot) dust grains. This is an unexpected result, as there is no obvious mechanism for removing the small grains. By varying the minimum size cutoff explicitly, an excellent fit is possible, but only if the cutoff size is set to 3.5 $\mu$m and the $p = 0$ model is used, as shown in Figure 5. Changing the cutoff size cannot produce a good fit if the porous or icy models are used (Figure 6). Modifying the slope of the size distribution can improve the fit (Figure 7), but cannot make the model consistent with the data.

Solid dust grains with a size of 3.5 $\mu$m have a $\beta$ of about

0.15, much less than is needed to remove the grains by radiation pressure. It therefore seems that the disk around $\epsilon$ Eri contains few grains smaller than about 3 $\mu$m, and radiation pressure from the star cannot explain this deficiency. Possible causes for this discrepancy are discussed in Section 7.

Recently, detailed modelling of $\epsilon$ Eri has been presented by Li, Lunine & Bendo (2003) who modelled the SED and SCUBA image using a porous dust model ($p = 0.9$, $q_{\text{ice}} = 0.0$), and were able to get an excellent fit. With this in mind, our results seem somewhat surprising, as they favour solid rather than porous grains, and fail to produce an acceptable fit at all unless grains with diameter smaller than 3.5 $\mu$m are excluded. The discrepancy arises because of several differences in the assumptions made within the two models. The most important difference is that Li et al. (2003) set a maximum grain size cutoff at a diameter of 2 cm, whereas in our modelling the maximum grain size is set to be 10 m. If the collisional cascade model is true, then the real size distribution will extend up to very large bodies (i.e. kilometre scale and bigger), but the limit of 10 m is chosen because bodies of this size and larger make a negligible contribution to the sub-mm flux (i.e. the longest wavelength data included in our fits), and so can be safely excluded from the model. This is not true of 2 cm bodies, as grains of around this size can make a very significant contribution the the flux at 850 $\mu$m. Similarly, Li et al. (2003) set an a priori limit on the minimum grain diameter at 2 $\mu$m; our finding that we must remove grains smaller than 3.5 $\mu$m is therefore in reasonable agreement with this (the remaining discrepancy is due to the fact that Li et al. (2003) allow the slope of the size distribution to be a free parameter, whereas in the models where we modified $D_{\text{min}}$, $q$ was fixed to be 11/6). Finally, Li et al. (2003) have a different spatial dust distribution, with a peak at 55 AU and FWHM of 30 AU, compared with the infinitely thin ring at 60 AU used in our model. The broad spatial distribution has not been considered here as it would make our SED fit worse. Because Li et al. (2003) set tight limits on the size distribution, the dust SED becomes quite sharply peaked, and a broad spatial distribution is needed to make the dust SED wide enough to fit all the points. Conversely, in our model the broad size distribution means that the model SED is already *too* wide, so a broad spatial distribution would only make things worse. Given the low signal to noise of the SCUBA image, a direct measurement of the width of the dust ring is not possible.

Dent et al. (2000) also modeled the $\epsilon$ Eri data, and were able to fit the SED using a modified blackbody. The fitted parameters indicated that the disk must contain large grains ($\sim 30$ $\mu$m), but this type of modelling does not constrain the composition or porosity of the dust grains.

## 6.4   Vega

The original estimate for the size of Vega was made by Aumann et al. (1984), who analysed special pointed observations made with *IRAS* after the discovery of a far-IR excess. The estimated diameter was 23 arcsec at 60 $\mu$m (corresponding to a radius of 90 AU). Subsequently, this data was reanalysed, giving a larger diameter of $35 \pm 5$ arcsec (135 AU) (van der Bliek, Prusti & Waters 1994, and references therein). This discrepancy is attributed to the fact the Aumann et al. did not account for the photospheric emis-
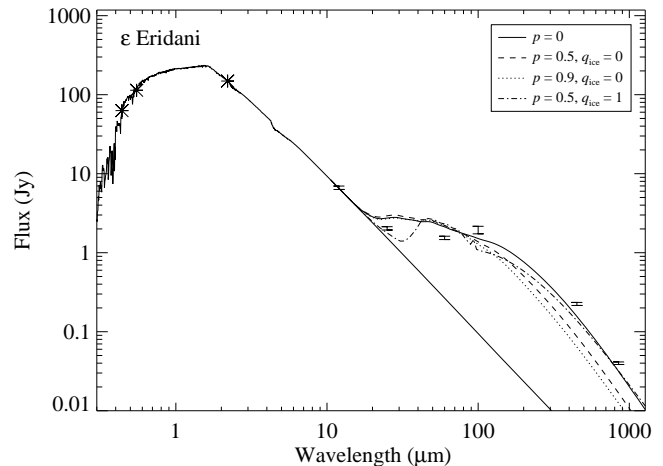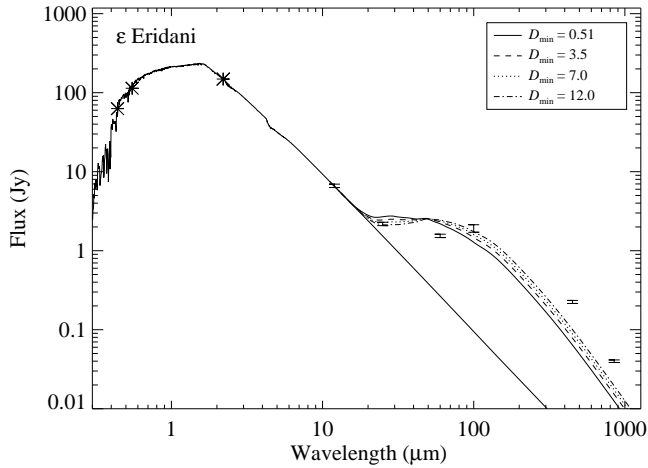


**Figure 4.** SED of $\epsilon$ Eri, with the ring radius set at 60 AU. Colour corrections for the *IRAS* data as plotted here were estimated from the $p = 0$ model.
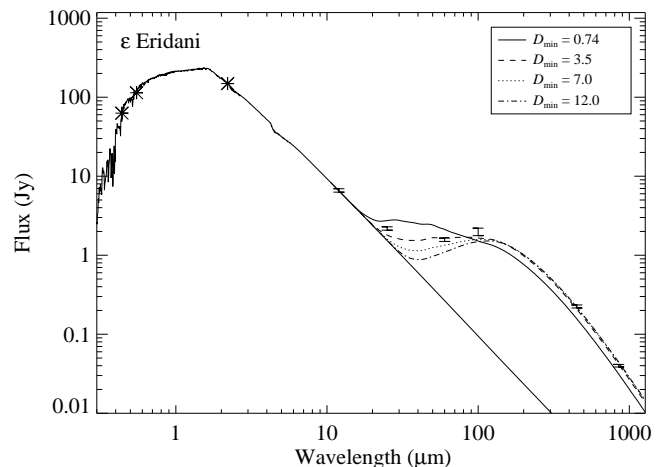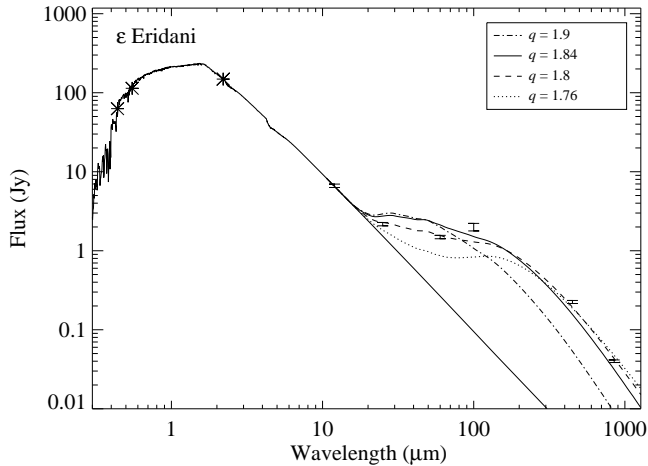


**Figure 5.** SED of $\epsilon$ Eri, with the ring radius set at 60 AU. Models show the effect of changing the minimum size cutoff when using solid grains ($p = 0$). Colour corrections for the *IRAS* data were estimated from the $D_{\text{min}} = 3.5$ $\mu$m model.

sion at 60 $\mu$m, and hence underestimated the extent of the excess emission. However, sub-mm observations made with SCUBA on the JCMT indicate a diameter of $24 \pm 3$ arcsec (Holland et al. 1998), similar to the original estimate from the *IRAS* data. At millimetre wavelengths, aperture synthesis imaging has been done using the Plateau de Bure interferometer (Wilner et al. 2002) and Owens Valley Radio Observatory (Koerner, Sargent & Ostroff 2001). Both of these observations suggested that the Vega disk is very clumpy, and found bright clumps at a distance of 9 arcsec (Plateau de Bure) and 12 arcsec (Owens Valley) from the central star. This could indicate a disk radius as small as 70 AU.

Given these observations, it is not obvious what the true size of the disk is, and so we were unable to fix this parameter in our model fits. Instead, we fitted different grain mod-
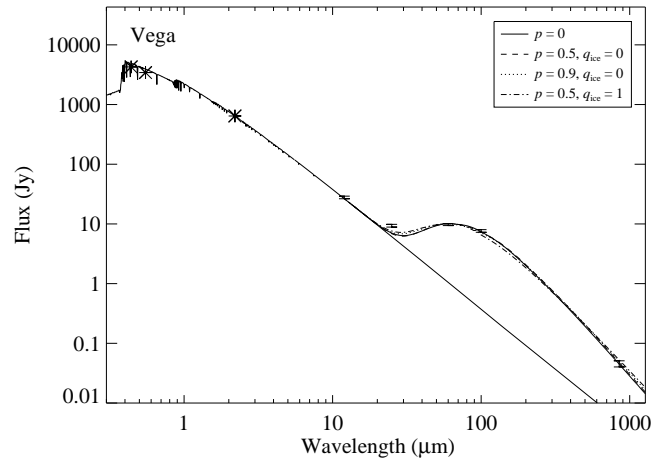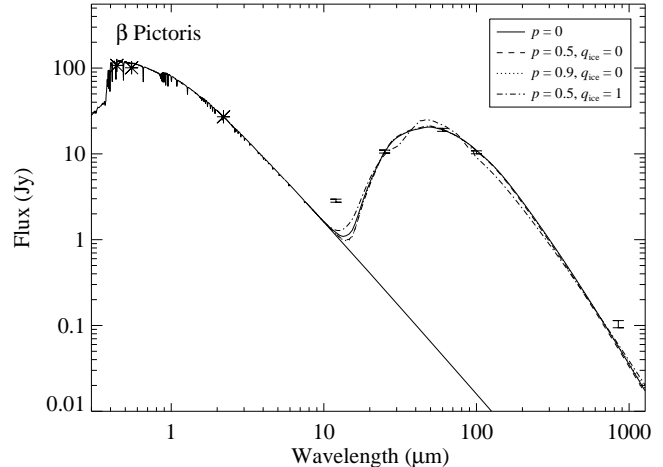
**Figure 6.** SED of $\epsilon$ Eri, with the ring radius set at 60 AU. Models show the effect of changing the minimum size cutoff when using porous grains ($p = 0.9$). Colour corrections for the *IRAS* data were estimated from the $D_{\min} = 3.5$ $\mu$m model.



**Figure 8.** SED of Vega and model fits to the data with ring radius as a free parameter. Colour corrections for the *IRAS* data as plotted here were estimated from the $p = 0$ model.



**Figure 7.** SED of $\epsilon$ Eri, with the ring radius set at 60 AU. Models show the effect of changing the slope of the size distribution ($q$). Colour corrections for the *IRAS* data were estimated from the $q = 1.8$ $\mu$m model.



**Figure 9.** SED of $\beta$ Pic and model fits to the data with ring radius as a free parameter. Colour corrections for the *IRAS* data as plotted here were estimated from the $p = 0$ model.

els with disk size as a free parameter. With this approach we find that all of the dust grain models fit equally well (Figure 8), but predict very different disk sizes. The porous grain models both have a fitted radius much larger than any of the observations, with the $p = 0.5$, $q_{\rm ice} = 0.0$ model suggesting a radius of $191 \pm 16$ AU, and the $p = 0.9$, $q_{\rm ice} = 0.0$ model giving $237 \pm 21$ AU. These models can therefore be rejected. However, the solid grain model ($p = 0.0$) gives a radius of $120 \pm 13$ AU, and the icy $p = 0.5$, $q_{\rm ice} = 1.0$ model gives $92 \pm 8$ AU, both of which are compatible with the observations. Without more detailed analysis of the structure observed in the disk, it is impossible to distinguish between these two options.

There is a small additional excess at 25 $\mu$m ($\sim 2$ Jy), which none of the models account for. This could either

be due to an additional warm dust component similar to that found for HR4796, or because the spatial distribution is broad, with dust at a range of distances from the star.

### 6.5 $\beta$ Pic

$\beta$ Pic is the most extensively studied Vega excess star, with observations in scattered light, mid-IR, far-IR, sub-mm. The system is not a ring, but a disk with dust at a variety of distances from the star. The system has been modelled in detail by Li & Greenberg (1998a), and our simpler model is not adequate to deal with the extended spatial structure of the disk. However, we have included $\beta$ Pic here in order to show the consequences when our model is applied to objects where the dust is not contained within a ring. The ring morphology is one of the key assumptions of our model, so it is

extremely important that we can determine whether or not this is true for unresolved objects.

To fit the SED, we used the same approach taken for Vega, i.e. we left the ring radius as a free parameter, and fitted each dust composition to the SED. The modelling shows that it is not possible to fit the observed SED with any single model regardless of what dust composition is chosen (Figure 9). This is a helpful result, in that it shows that we are able to distinguish between a disk and a ring morphology purely from the SED. However, this modelling reveals little else about the composition and size distribution of dust grains in $\beta$ Pic.

## 6.6 HD141569

HD141569 has a resolved circumstellar disk, first directly detected in near-IR scattered light images (Augereau et al. 1999a; Weinberger et al. 1999), and subsequently resolved in mid-IR thermal emission (Fisher et al. 2000; Mouillet et al. 2001; Marsh et al. 2002). Most recently, the disk has been observed with the ACS coronagraph (Clampin et al. 2002), revealing that the structure observed in the disk is probably caused by a tidal interaction with a bound binary system at a projected distance of around 1000 AU. The age of the system has been estimated to be $5 \pm 3$ Myr (Weinberger et al. 2000), making it one of the youngest stars in our sample. However, despite its youth the disk appears to be in a collisional cascade, as modelling shows that it contains small dust grains which must leave the system on a very short timescale (Fisher et al. 2000).

The mid-IR imaging shows that the overall size of the disk is around 100 AU, but the emission is produced at a range of distances from the star from 20 AU outwards (Marsh et al. 2002). This is also apparent from our SED modelling, as no model can simultaneously fit all the data (Figure 10). When only the long wavelength points are fitted (i.e. only the cooler, outer parts of the disk), the fitted radius is about 50 AU if solid ($p = 0$) or icy ($p = 0.5$, $q_{ice} = 1.0$) grains are used, but 114 AU for porous grains ($p = 0.9$, $q_{ice} = 0.0$). This indicates that the thermal emission is probably produced by porous grains, in agreement with the modelling done by Li & Lunine (2003b).

## 6.7 HD109085

HD109085 is clearly detected in the sub-mm, indicating that the *IRAS* association is real. However, no model can simultaneously fit all of the data (Figure 11). This indicates that there must be dust at a variety of distances from the star, as is the case for $\beta$ Pic and HD141569. For our fitted model, the *IRAS* 12 and 25 $\mu$m points have not been included, so the fitted radius reflects the size of the coolest parts of the disk, i.e. the disk's overall extent. This gives a result of 180 AU, which at a distance of 18.2 pc gives an angular radius of 9.9 arcsec. This is more extended than the SCUBA beam, so our flux estimate is probably smaller that the true flux by a factor of $\sim 2$ (Table 3). Given the size and brightness of the disk, it should be possible to fully map HD109085 with SCUBA, and such observations are currently being performed (Wyatt et al. in preparation).
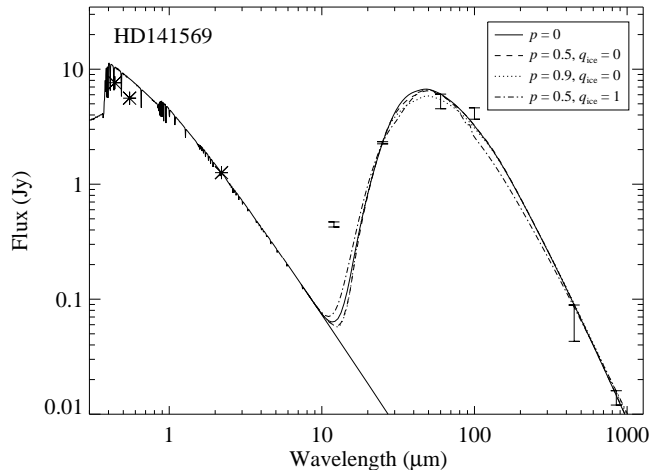


**Figure 10.** SED of HD14159 with model fits for different grain compositions. The ring radius is a free parameter in each case. Colour corrections for the *IRAS* data as plotted here were estimated from the $p = 0$ model.
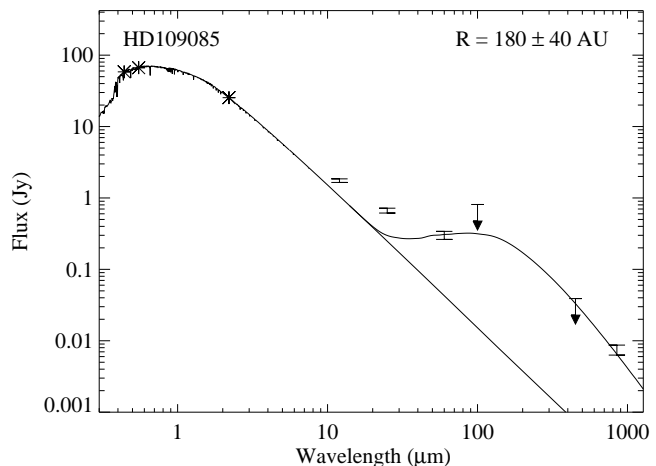


**Figure 11.** SED of HD109085 with model fit to the data. Ring radius is a free parameter. Upper limits are 3 sigma.

## 6.8 HD38393

HD38393 is extremely faint in the sub-mm, and is only detected at the 2.4 sigma level. The modelling produces a good fit to the SED (Figure 12), but with a disk radius of $200 \pm 50$ AU for solid dust grains. At the distance of HD38393 (9.0 pc), this corresponds to a radius of 22 arcsec. This would place most of the flux outside the SCUBA beam (even though the extended photometry mode was used), implying that the true flux at 850 $\mu$m is much higher than the measured flux. In fact, if this radius is correct we would only detect emission if the source is edge on. Revising our estimate of the 850 $\mu$m flux results in a still larger fitted radius (because a higher sub-mm flux indicates a cooler disk), and so does not resolve this problem. Nor does choosing a different dust composition, as porous grains tend to be warmer
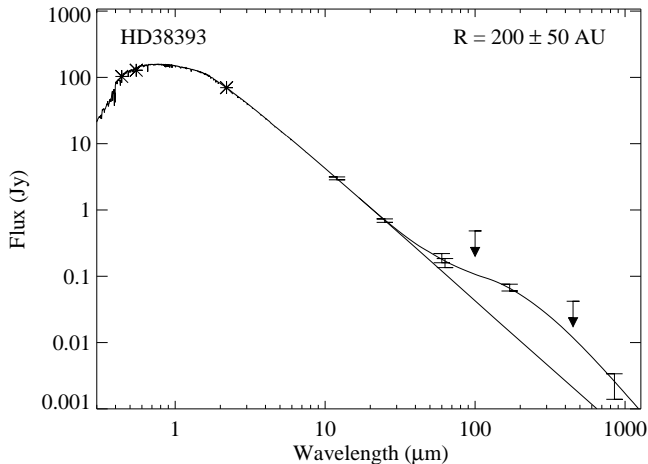
**Figure 12.** SED of HD38393 with model fit to the data. The *ISO* 60 $\mu$m point has been offset to the right to distinguish it from the *IRAS* 60 $\mu$m point. Upper limits are 3 sigma.
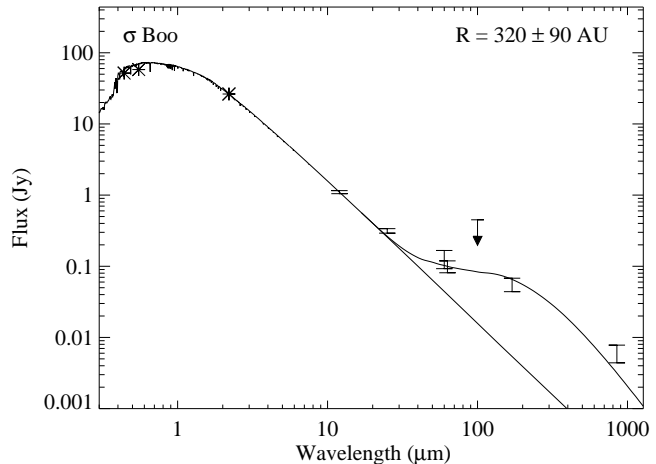


**Figure 13.** SED of $\sigma$ Boo. The *ISO* 60 $\mu$m point has been offset to the right to distinguish it from the *IRAS* 60 $\mu$m point. Upper limits are 3 sigma.

than solid grains, and so also increase the estimated disk size.

Given the low significance of the detection, it is possible that the 850 $\mu$m detection is either spurious, or caused by a background galaxy. Using source counts of galaxies detected in blank fields (e.g. Figure 11 in Scott et al. 2002), we find there is a 6 per cent probability that a 2.4 mJy background source will fall into the beam of SCUBA in extended photometry mode (which is sensitive over a 300 arcsec$^2$ area). Habing et al. (2001) also concluded that their 170 $\mu$m detection is likely to be due to a background galaxy, given the low flux and the galaxy number counts at that wavelength. However, an alternative explanation is that the estimate of the disk size is wrong: the difficulty fitting the SED of $\epsilon$ Eri may indicate that our model is generally unreliable for cool stars, and hence the true size of the disk could be smaller than 200 AU. This would mean that the disk is deficient in small grains compared with our model.

### 6.9    $\sigma$ Boo

Excess sub-mm emission from $\sigma$ Boo was detected at the 3.6 sigma level, with a flux of 6.7 mJy. However, the best fitting model gives a disk radius of $320 \pm 90$ AU, which corresponds to an angular radius of 20 arcsec, implying that most of the 850 $\mu$m flux would be outside the SCUBA beam even in extended photometry mode. In addition, the best fitting model predicts a much lower 850 $\mu$m flux than the observed value. As is the case for HD38393, there is no model which is consistent with both the SED and the spatial constraints given by the SCUBA beam size. The problem is unlikely to be caused by errors in the far-IR data: the *IRAS* and *ISO* results are entirely consistent, and the *ISO* 170 $\mu$m observation has a beam radius of about 45 arcsec, so all the flux would be detected with *ISO*, even if the disk really is very large.

Habing et al. (2001) considered the possibility that their *ISO* detection at 60 and 170 $\mu$m was due to a background galaxy. They concluded that the excess was probably

real, but could not rule out contamination by a background source. A background galaxy with a flux of 6.7 mJy is unlikely to fall into the SCUBA beam by chance alone (1 per cent probability), but as $\sigma$ Boo was selected on the basis of a far-IR excess, contamination by a background source becomes more likely. The alternative explanation is that $\sigma$ Boo is deficient in small grains, which would reconcile the modelling results with the SCUBA beam size.

### 6.10    HD48682

HD48682 is a quoted as visual binary in the Washington double star catalogue with a separation of 34 arcsec. However the two stars cannot be physically associated due to their differing proper motions, and it appears that HD48682B is in fact a background object. Given that the separation of the two components is similar to the *IRAS* beam size, it is not obvious whether the photosphere of the secondary will contribute to the *IRAS* fluxes or not. The *IRAS* beam is different at each wavelength, as the diffraction limit is much smaller at 12 $\mu$m than it is at 100 $\mu$m. This means that the secondary photosphere may only contribute to the measured fluxes at longer wavelengths. In addition, it is very difficult to estimate the brightness of the secondary at *IRAS* wavelengths, because the star is most likely an M star and only optical photometry is available. A small uncertainty in the effective temperature therefore causes a large error in the estimated mid-IR flux. A K band image would resolve this problem, but unfortunately the secondary star is saturated on 2MASS images, so a dedicated observation would be required. Aumann & Probst (1991) made ground based observations of HD48682 at 10 $\mu$m, and concluded that the 12 $\mu$m excess comes from > 6 arcsec from the primary and is consistent with the flux from the secondary, but that the secondary photosphere cannot account for the large 60 $\mu$m excess. Our detection with SCUBA confirms that the 60 $\mu$m *IRAS* excess is associated with the primary and not the secondary, but the source of the 12 and 25 $\mu$m excess is not clear.
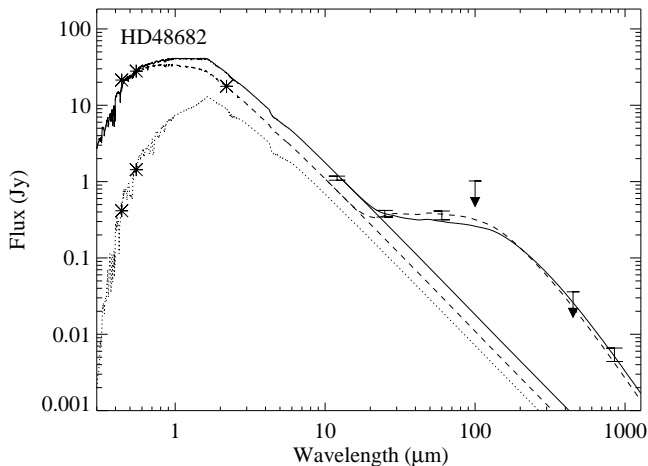
**Figure 14.** SED of HD48682, with model fit to the data. Asterisks show optical and near-IR photometry, *IRAS* and SCUBA data are shown with error bars. The photospheric flux from the primary, and the best fit model assuming that only the primary contributes to the *IRAS* fluxes are shown with dashed lines. The secondary is shown with a dotted line. Solid lines show the combined photospheric flux, and combined photospheric flux plus best fit model assuming that the secondary does contribute to the *IRAS* fluxes. Upper limits are $3\sigma$.

Figure 14 shows the SED of HD48682, and the best fit model. The modelling has been done in two ways, with and without the secondary included in the photosphere subtraction (assuming a spectral type M0). At 12 $\mu$m, the IRAS flux is more than the photosphere of the primary, which could either be due to circumprimary emission at > 6 arcsec, or flux from the secondary. At 25 $\mu$m, the *IRAS* flux is more than the combined flux from primary and secondary, indicating that there is definitely emission by dust at this wavelength. There is a large excess at 60 $\mu$m, and the secondary photosphere could only make a small contribution even if it is within the beam. The modelling results are better if the secondary is included in the photosphere subtraction (reduced $\chi^2 = 3.1$, verses 7.0 if the secondary is not included). If the secondary is not included in the subtraction, the estimated radius is $71 \pm 15$ AU, whereas if the secondary is included, the estimated radius is $110 \pm 21$ AU. If the larger value is true, the projected radius would be 6.7 arcsec, so the disk could be marginally resolved with SCUBA mapping. The shape of the fitted model indicates that there would be only a small excess at 18 $\mu$m, so resolved ground based imaging would be difficult.

### 6.11 HD207129

HD207129 is not detected in our reduction of archived SCUBA measurements, but because there are *ISO* measurements at 170 $\mu$m a model fit is possible, and the SCUBA upper limit also helps to constrain this fit. The SED and model fit are shown in Figure 15. The fitted size of the disk is $260 \pm 50$ AU, which corresponds to an angular radius of 17 arcsec. Since this is larger than the SCUBA beam a significant fraction of the flux would not have been detected, and the quoted upper limit on the 850 $\mu$m flux may actu-
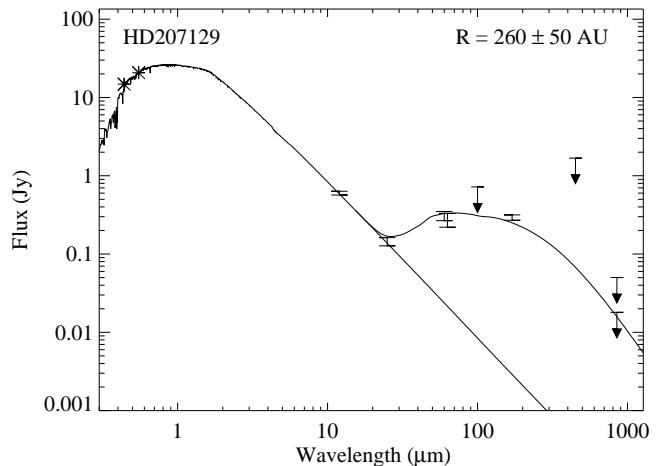


**Figure 15.** SED of HD207129. The *ISO* 60 $\mu$m point has been offset to the right to distinguish it from the *IRAS* 60 $\mu$m point. Upper limits are 3 sigma. The lower data point at 850 $\mu$m is the result if the source is unresolved, the upper point is the result if the source is resolved but with a radius smaller than 20 arcsec.

ally be lower than the true flux. HD207129 was observed in both photometry mode and map mode, and the quoted upper limit of < 0.018 Jy is based on both sets of measurements. If just the mapping data is used, then an integrated flux over a 20 arcsec radius aperture can be calculated. This method gives a flux < 0.05 Jy (3 sigma).

## 7 DISCUSSION

The most striking result of our modelling is that there is a large diversity in dust grain compositions between different disks. A simple explanation for this result is that dust grain composition may vary with age. The modelling of HD141569 and HR4796 (age 5 and 8 Myr respectively) indicates high porosity grains ($p = 0.9$), as does the previous modelling of $\beta$ Pic (age 20 Myr) done by Li & Greenberg (1998a). However, solid grains are indicated for Fomalhaut and Vega (ages 150 and 350 Myr). It may be that the older stars have less porous grains because the collisional cascade has reprocessed the initially fluffy grains into a more solid form. An alternative explanation is that the change in porosity is due to the effects of stellar radiation on the dust, as suggested to explain the differences between the porosity of long and short period comets (Mukai & Fechtig 1983; Li & Greenberg 1998b). Clearly, a larger sample of resolved disks is required to confirm this trend.

The failure of our basic model to fit the SED of $\epsilon$ Eri is extremely interesting, and it's important to determine what is causing the poor fit. There are essentially two possibilities: either there is an unknown physical effect which is modifying the size distribution in the particular case of $\epsilon$ Eri, or else the size distribution model we have assumed is intrinsically wrong.

$\epsilon$ Eri is known to have a planet (Hatzes et al. 2000), with a semi-major axis of 3.4 AU and a mass of around 2 Jupiter masses (assuming an inclination of 25° as measured by Greaves et al., 1998). This planet in unlikely to affect the

dust size distribution at 60 AU, because of its small orbital radius. However, a planet with a large semi-major axis has been inferred from the existence of clumps within the dust disk (Quillen & Thorndike 2002). If this planet is real, then dynamical effects are clearly very important in shaping the disk, and this would undoubtedly affect the size distribution of the dust (Wyatt 2003, submitted).

The alternative explanation is that the discrepancy is not due to an external influence, but that a more accurate treatment of the dust grain size distribution in a collisional cascade is needed to account for the SED. More detailed size distribution models allow the grain strength to vary with grain size, and account for the the effects of removing small grains on the overall size distribution (Campo Bagatin et al. 1994; Durda & Dermott 1997). For $\beta$ Pic, extensive numerical models of this type have been produced, both for the inner disk (Thébault, Augereau & Beust, submitted) and for the outer disk (Krivov, Mann & Krivova 2000). Both of these studies show significant deviation from the theoretical size distribution used in this paper. This suggests that a more rigorous treatment of the collisional cascade in $\epsilon$ Eri would also give a significantly different size distribution. However, it is not obvious that this would produce a better fit to the SED (i.e. that the new size distribution would have few grains smaller than 3 $\mu$m). In fact, according to Campo Bagatin et al. (1994) we should expect an enhancement of grains just above the blowout radius as they are less likely to be destroyed by collisions, which would make the problem worse. Conversely, the modelling of $\beta$ Pic's outer disk by Krivov et al. (2000) suggests a reduction in the number of grains just above the blowout limit, because they are destroyed by small, fast moving grains as they are ejected from the system by radiation pressure. However, as the stellar luminosity is much lower for $\epsilon$ Eri, this mechanism is likely to be less important. Only detailed modelling specific to $\epsilon$ Eri's dust disk can answer this question.

The new sub-mm data significantly expands the sample of true Vega excess stars detected at this wavelength. Regardless of the dust properties, we are able to distinguish between a disk morphology and a ring morphology. Out of the five new objects, only HD109085 is disk like, indicating that this type is less common than the ring like structure observed around Fomalhaut and $\epsilon$ Eri.

One of the main aims of this work was to determine the size of an unresolved disk from just its SED. However, the modelling of resolved targets has shown that this may not be possible. The large diversity in dust properties for the resolved disks mean that we cannot make a reliable assumption as to the composition of the grains in an unresolved disk. In addition, the poor fit to $\epsilon$ Eri's SED shows that the model may not in general contain all of the physics necessary to account for the observations. Our estimates of the disk size are based on assumption that the dust grains are solid (as for Fomalhaut), but if the grain properties are different, then the size estimates will be incorrect.

Future progress in this field depends on spatially resolving disks, as this allows a direct measure of disk size and thus measurements of the dust composition. Our results indicate that there are probably a few more targets that can be resolved using SCUBA, given sufficient integration time. Also, ground based mid-IR observations also have the ability to resolve some disks. However, large numbers of resolved disks may have to wait until SIRTF and SOFIA become available.

## 8    CONCLUSION

We have presented new observations and modelling of Vega excess disks with sub-mm data. Our observations expand the sample of Vega excess stars detected in the sub-mm from 5 to 10, with a further 4 objects which were not detected but have useful upper limits. We have fitted the observed SEDs with models based on realistic dust grain composition and size distribution. We find that dust grain composition varies significantly between different objects, with younger disks having more porous grains. For $\epsilon$ Eri, our model fails to fit the data unless there are less small grains in the system than expected from a collisional cascade. This discrepancy may be due to an inadequacy in our model of the size distribution, or the result of an external influence such as a planet. For the unresolved targets, disk size is estimated assuming solid dust grains, but given the observed diversity in dust composition and the problems fitting $\epsilon$ Eri, these size estimates may not be reliable.

This paper has been typeset from a TeX/ LaTeX file prepared by the author.

## REFERENCES

Archibald E. N., Wagg J. W., Jenness T., 2000. http://www.jach.hawaii.edu/JACdocs/JCMT/SCD/SN/002.2/

Augereau J. C., Lagrange A. M., Mouillet D., Ménard F., 1999a, A&A, 350, L51

Augereau J. C., Lagrange A. M., Mouillet D., Papaloizou J. C. B., Grorod P. A., 1999b, A&A, 348, 557

Aumann H. H., Beichman C. A., Gillett F. C., de Jong T., Houck J. R., Low F. J., Neugebauer G., Walker R. G., et al., 1984, ApJ, 278, L23

Aumann H. H., Probst R. G., 1991, ApJ, 368, 264

Backman D. E., Paresce F., 1993, in Protostars and Planets III, pp. 1253–1304

Barrado y Navascués D., Stauffer J. R., Song I., Caillault J.-P., 1999, ApJ, 520, L123

Beichman C. A., Neugebauer G., Habing H. J., Clegg P. E., Chester T. J., eds., 1988, Infrared astronomical satellite (IRAS) catalogs and atlases. Volume 1: Explanatory supplement

Bohren C. F., Huffman D. R., 1983, Absorption and scattering of light by small particles. New York: Wiley, 1983

Campo Bagatin A., Cellino A., Davis D. R., Farinella P., Paolicchi P., 1994, Planet. Space Sci., 42, 1079

Clampin M., Krist J. E., Golimowski D. A., Ardila D. R., Bartko F., Benítez N., Blakeslee J. P., Bouwens R., et al., 2002, American Astronomical Society Meeting, 201, 0

Dent W. R. F., Walker H. J., Holland W. S., Greaves J. S., 2000, MNRAS, 314, 702

Dohnanyi J. W., 1969, J. Geophys. Res., 74, 2531

Dominik C., The Hjhvega Consortium, 1997, Ap&SS, 255, 103

Dunne L., Eales S. A., 2001, MNRAS, 327, 697

Durda D. D., Dermott S. F., 1997, Icarus, 130, 140

Fajardo-Acosta S. B., Stencel R. E., Backman D. E., Thakur N., 1999, ApJ, 520, 215

Fisher R. S., Telesco C. M., Piña R. K., Knacke R. F., Wyatt M. C., 2000, ApJ, 532, L141

Gray R. O., Corbally C. J., 1994, AJ, 107, 742

Greaves J. S., Holland W. S., Moriarty-Schieven G., Jenness T., Dent W. R. F., Zuckerman B., McCarthy C., Webb R. A., et al., 1998, ApJ, 506, L133

Greenberg J. M., 1982, in IAU Colloq. 61: Comet Discoveries, Statistics, and Observational Selection, pp. 131–163

—, 1998, A&A, 330, 375

Habing H. J., Dominik C., Jourdain de Muizon M., Laureijs R. J., Kessler M. F., Leech K., Metcalfe L., Salama A., et al., 2001, A&A, 365, 545

Hatzes A. P., Cochran W. D., McArthur B., Baliunas S. L., Walker G. A. H., Campbell B., Irwin A. W., Yang S., et al., 2000, ApJ, 544, L145

Heap S. R., Lindler D. J., Lanz T. M., Cornett R. H., Hubeny I., Maran S. P., Woodgate B., 2000, ApJ, 539, 435

Holland W. S., Greaves J. S., Dent W. R. F., Wyatt M. C., Zuckerman B., Webb R. A., McCarthy C., Coulson I. M., et al., 2003, ApJ, 582, 1141

Holland W. S., Greaves J. S., Zuckerman B., Webb R. A., McCarthy C., Coulson I. M., Walther D. M., Dent W. R. F., et al., 1998, Nature, 392, 788

Jayawardhana R., Fisher S., Hartmann L., Telesco C., Pina R., Fazio G., 1998, ApJ, 503, L79+

Jayawardhana R., Holland W. S., Kalas P., Greaves J. S., Dent W. R. F., Wyatt M. C., Marcy G. W., 2002, ApJ, 570, L93

Jourdain de Muizon M., Laureijs R. J., Dominik C., Habing H. J., Metcalfe L., Siebenmorgen R., Kessler M. F., Bouchet P., et al., 1999, A&A, 350, 875

Jura M., 1991, ApJ, 383, L79+

Kalas P., Graham J. R., Beckwith S. V. W., Jewitt D. C., Lloyd J. P., 2002, ApJ, 567, 999

Koerner D. W., Ressler M. E., Werner M. W., Backman D. E., 1998, ApJ, 503, L83+

Koerner D. W., Sargent A. I., Ostroff N. A., 2001, ApJ, 560, L181

Krivov A. V., Mann I., Krivova N. A., 2000, A&A, 362, 1127

Lachaume R., Dominik C., Lanz T., Habing H. J., 1999, A&A, 348, 897

Lagrange A. ., Backman D. E., Artymowicz P., 2000, in Protostars and Planets IV, pp. 639+

Lang K. R., 1992, Astrophysical Data I. Planets and Stars. Springer-Verlag, Berlin Heidelberg New York

Li A., Greenberg J. M., 1997, A&A, 323, 566

—, 1998a, A&A, 331, 291

—, 1998b, A&A, 338, 364

Li A., Lunine J. I., 2003a, ApJ, 590, 368

—, 2003b, ApJ, 594, 987

Li A., Lunine J. I., Bendo G. J., 2003, ApJ, 598, L51

Lisse C., Schultz A., Fernandez Y., Peschke S., Ressler M., Gorjian V., Djorgovski S. G., Christian D. J., et al., 2002, ApJ, 570, 779

Marsh K. A., Silverstone M. D., Becklin E. E., Koerner D. W., Werner M. W., Weinberger A. J., Ressler M. E., 2002, ApJ, 573, 425

Moshir M., Kopan G., Conrow T., McCallon H., Hacking P., Gregorich D., Rohrbach G., Melnyk M., et al., 1990, BAAS, 22, 1325

Mouillet D., Lagrange A. M., Augereau J. C., Ménard F., 2001, A&A, 372, L61

Mukai T., Fechtig H., 1983, Planet. Space Sci., 31, 655

Piétu V., Dutrey A., Kahane C., 2003, A&A, 398, 565

Pollack J. B., Hollenbach D., Beckwith S., Simonelli D. P., Roush T., Fong W., 1994, ApJ, 421, 615

Quillen A. C., Thorndike S., 2002, ApJ, 578, L149

Schneider G., Smith B. A., Becklin E. E., Koerner D. W., Meier R., Hines D. C., Lowrance P. J., Terrile R. J., et al., 1999, ApJ, 513, L127

Scott S. E., Fox M. J., Dunlop J. S., Serjeant S., Peacock J. A., Ivison R. J., Oliver S., Mann R. G., et al., 2002, MNRAS, 331, 817

Smith B. A., Terrile R. J., 1984, Science, 226, 1421

Song I., Caillault J.-P., Barrado y Navascués D., Stauffer J. R., 2001, ApJ, 546, 352

Song I., Caillault J.-P., Barrado y Navascués D., Stauffer J. R., Randich S., 2000, ApJ, 533, L41

Stauffer J. R., Hartmann L. W., Barrado y Navascues D., 1995, ApJ, 454, 910

Sylvester R. J., Dunkin S. K., Barlow M. J., 2001, MNRAS, 327, 133

Sylvester R. J., Skinner C. J., Barlow M. J., Mannings V., 1996, MNRAS, 279, 915

van der Bliek N. S., Prusti T., Waters L. B. F. M., 1994, A&A, 285, 229

Weinberger A. J., Becklin E. E., Schneider G., Smith B. A., Lowrance P. J., Silverstone M. D., Zuckerman B., Terrile R. J., 1999, ApJ, 525, L53

Weinberger A. J., Rich R. M., Becklin E. E., Zuckerman B., Matthews K., 2000, ApJ, 544, 937

Wilner D. J., Holman M. J., Kuchner M. J., Ho P. T. P., 2002, ApJ, 569, L115

Wyatt M. C., Dent W. R. F., 2002, MNRAS, 334, 589

Wyatt M. C., Dermott S. F., Telesco C. M., Fisher R. S., Grogan K., Holmes E. K., Piña R. K., 1999, ApJ, 527, 918

Zuckerman B., Becklin E. E., 1993, ApJ, 414, 793